2D Materials

PAPER • OPEN ACCESS

Influence of the substrate material on the optical properties of tungsten diselenide monolayers

To cite this article: Sina Lippert *et al* 2017 *2D Mater.* **4** 025045

2D Materials

OPEN ACCESS

CrossMark

RECEIVED
10 October 2016

REVISED
20 December 2016

ACCEPTED FOR PUBLICATION
20 January 2017

PUBLISHED
9 March 2017

PAPER

Influence of the substrate material on the optical properties of tungsten diselenide monolayers

Sina Lippert[1,4], Lorenz Maximilian Schneider[1,4], Dylan Renaud[1], Kyung Nam Kang[2], Obafunso Ajayi[3], Jan Kuhnert[1], Marc-Uwe Halbich[1], Oday M Abdulmunem[1], Xing Lin[1], Khaleel Hassoon[1], Saeideh Edalati-Boostan[1], Young Duck Kim[3], Wolfram Heimbrodt[1], Eui-Hyeok Yang[2], James C Hone[3] and Arash Rahimi-Iman[1,5]

1 Department of Physics and Materials Sciences Center, Philipps-Universität Marburg, Marburg 35032, Germany
2 Department of Mechanical Engineering, Stevens Institute of Technology, Hoboken, NJ 07030, United States of America
3 Department of Mechanical Engineering, Columbia University, New York, NY 10027, United States of America
4 These authors have contributed equally.
5 Author to whom any correspondence should be addressed.

E-mail: a.r-i@physik.uni-marburg.de

Keywords: transition-metal dichalcogenide, optical properties, substrate materials, 2D excitons

Supplementary material for this article is available online

Abstract

Monolayers of transition-metal dichalcogenides such as WSe_2 have become increasingly attractive due to their potential in electrical and optical applications. Because the properties of these 2D systems are known to be affected by their surroundings, we report how the choice of the substrate material affects the optical properties of monolayer WSe_2. To accomplish this study, pump-density-dependent micro-photoluminescence measurements are performed with time-integrating and time-resolving acquisition techniques. Spectral information and power-dependent mode intensities are compared at 290 K and 10 K for exfoliated WSe_2 on SiO_2/Si, sapphire (Al_2O_3), hBN/Si_3N_4/Si, and MgF_2, indicating substrate-dependent appearance and strength of exciton, trion, and biexciton modes. Additionally, one CVD-grown WSe_2 monolayer on sapphire is included in this study for direct comparison with its exfoliated counterpart. Time-resolved micro-photoluminescence shows how radiative decay times strongly differ for different substrate materials. Our data indicates exciton–exciton annihilation as a shortening mechanism at room temperature, and subtle trends in the decay rates in correlation to the dielectric environment at cryogenic temperatures. On the measureable time scales, trends are also related to the extent of the respective 2D-excitonic modes' appearance. This result highlights the importance of further detailed characterization of exciton features in 2D materials, particularly with respect to the choice of substrate.

Introduction

2D materials such as MoS_2, WS_2 and WSe_2 belong to the family of transition metal dichalcogenides (TMDs) which have recently attracted a vast amount of attention for their remarkable and unusual properties. As a semiconducting alternative to graphene, TMDs have promising applications in photonics [1, 2], optoelectronics [3, 4], valleytronics [5], field effect transistors [6], gas sensors [7], mechanical resonators [8, 9] and energy storage devices [10].

In 1970, Consadori and Frindt produced bilayer WSe_2 for the first time by mechanical exfoliation [11]. Today, the 'scotch tape method' is the most used method [12–16] to prepare monolayers (MLs) of WSe_2 from its bulk counterpart. However, WSe_2 layers have been also fabricated using chemical exfoliation [17–19], chemical vapor deposition (CVD) [20–24], metal-organic chemical vapor deposition (MOCVD) [25], hydrothermal exfoliation [26], liquid exfoliation [27–29], and physical vapor deposition [30, 31]. Due to the existence of these various fabrication techniques, the focus has now shifted to the production of high-quality MLs [16, 32, 33].

Reflection contrast [34–36], transient absorption [35], time-integrated photoluminescence (PL) [37, 38] and time-resolved photoluminescence (TRPL) [39, 40] experiments, have been performed to study the emission properties of WSe_2. In prior studies on WSe_2, layers were deposited on SiO_2/Si substrates [41, 42], sapphire [43, 44], graphene [45], and fused silica (quartz) [34, 46] or sandwiched between layers of hBN [47]. Based on the literature on WSe_2 and its properties, it has been identified as an ideal/suitable testbed for investigating the impact of substrate properties on its excitonic species. In addition, WSe_2 possesses good luminescence at room temperature (RT) and reasonable emission at low temperatures (LT). Finally, prior studies have confirmed the existence of excitons, trions [34, 38, 48] and more recently even biexcitons [49] and dark excitons [50]. Ultimately, the role of the dielectric environment and surface properties on excitons shall be unravelled in detail soon. Nevertheless, first studies indicate resonance shifts due to surface quality [51], strain and tensions in the material [38, 52, 53], and water moisture [54]. Others indicate that the excitonic resonance remains fixed even though the dielectric environment is altered [55]. This process is understood as an expected change of binding energy being compensated by a simultaneous bandgap renormalization [56] which can take place in WSe_2 [33, 57].

To date, a decisive comparison of ML samples showing the effect of the substrate material on a single type of ML material's emission signatures, on its time-dependent emission characteristics and on its Raman spectra has not yet been performed. Herein, we investigate time-integrated μPL spectra and corresponding time-resolved emission of ML WSe_2 (as a representative of this material class) using exfoliated WSe_2 isolated on SiO_2, sapphire, MgF_2 and hBN/Si_3N_4, together with a CVD-grown WSe_2 ML on sapphire, at RT and at 10 K, in order to show strong similarities and distinct differences in the emission pattern based on the substrate-material choice.

Experiment

ML samples

Mechanically exfoliated WSe_2 MLs have been transferred onto n-type SiO_2(300 nm)/Si, sapphire, multilayer-hBN (>10 nm) on Si_3N_4(75 nm)/Si and MgF_2 substrates and studied as prepared (for details on the sample fabrication see methods section). Although suggestions were made in the literature for the improvement of optical properties for ML materials by chemical treatment [58] and for mechanically stacked systems [59], a decisive comparison requires untreated samples to be investigated, which were fabricated under similar circumstances using the same procedures. Additionally, WSe_2 growth was conducted via a low pressure CVD process on a sapphire substrate. The detailed conditions of growth are similar to the growth condition of WS_2 reported elsewhere [60, 61]. This growth technique produced both millimeter-sized polycrystalline WSe_2 MLs and single crystalline WSe_2.

Here, the choice of substrates has been made for various reasons. Most importantly, a comparison of common transparent and opaque materials is desired. The chosen materials all exhibit a different refractive index, ranging from 1.38 to 2.2 (see table 1, and table SI.2 in the supporting information for further details). While oxidized Si (SiO_2 on Si) has become the standard platform for the investigation of 2D materials, other materials such as sapphire (Al_2O_3) and MgF_2 are becoming increasingly attractive due to their transparency. Combined with large area ML coverage by epitaxy (such as CVD), transparent materials can enhance the applicability of ML materials in optical devices while simultaneously giving access to experiments which require a transmission geometry. Taking into account the recent hunt for alternatives to SiO_2, Si_3N_4 has also been considered. It was recently introduced as a substrate material with improved optical contrast when used as a sub-100 nm layer on Si [67]. However, due to the potential of multi-layer hBN as an atomically smooth buffer layer [59], Si_3N_4 has been covered with exfoliated hBN to restore WSe_2's optical properties by preventing ML corrugation as a result of substrate surface roughness.

Microscopic pictures of the measured WSe_2 ML flakes on different substrates are shown in figure 1. The micrograph in figure 1(a) was recorded using a 100× magnification objective, while b through e were recorded with a 20× objective. In order to characterize the layer numbers, the optical contrast was evaluated along the path depicted in the figure as a yellow line. For this, the open-source software ImageJ was used [36]. The resulting cross sections are shown underneath the respective micrographs in figure 1. The steps are clearly visible in the cross section and were used to identify the ML sections [36]. The respective ML sections have been marked together with bulk and hBN sections (see figure 1). WSe_2 MLs have also been verified by Raman spectroscopy and μPL, which show the Raman signature and spectral features of ML WSe_2 for all investigated samples (for Raman data, see figures SI.1 and SI.2 in the supporting information (stacks.iop.org/TDM/4/025045/mmedia)).

Experimental setup

The micro-photoluminescence (μPL) and time-resolved (TR) μPL (in the following simply referred to as TRPL) measurements were performed with a pulsed Titanium-Sapphire (Ti:Sa) laser with a tuneable emission wavelength of 700–1000 nm, a pulse duration of 100 fs and a repetition rate of 80 MHz. The light from the laser was frequency doubled by nonlinear optics to provide an excitation wavelength of 445 nm. A schematic diagram of our optical setup to perform μPL measurements is shown in figure 2.

The samples were mounted onto the cold-finger of a continuous flow cryostat, where temperature T could be varied between 10 K and 290 K using a cooling system with liquid helium. The power-dependent μPL and

Table 1. Sample list.

Substrate/monolayer material	Preparation method	Refractive index of substrate at 750 nm	Reference (www.refractiveindex.info)
SiO_2/WSe_2	Exfoliated	1.474	Gao *et al* [62]
Sapphire/WSe_2	Exfoliated	1.762	Malitson and Dodge [63]
Sapphire/WSe_2	CVD	1.762	Malitson and Dodge [63]
MgF_2/WSe_2	Exfoliated	1.377	Dodge [64]
Si_3N_4/hBN/WSe_2	Exfoliated	2.017(Si_3N_4)/2.200(hBN)	Philipp [65]/Gielisse *et al* [66]

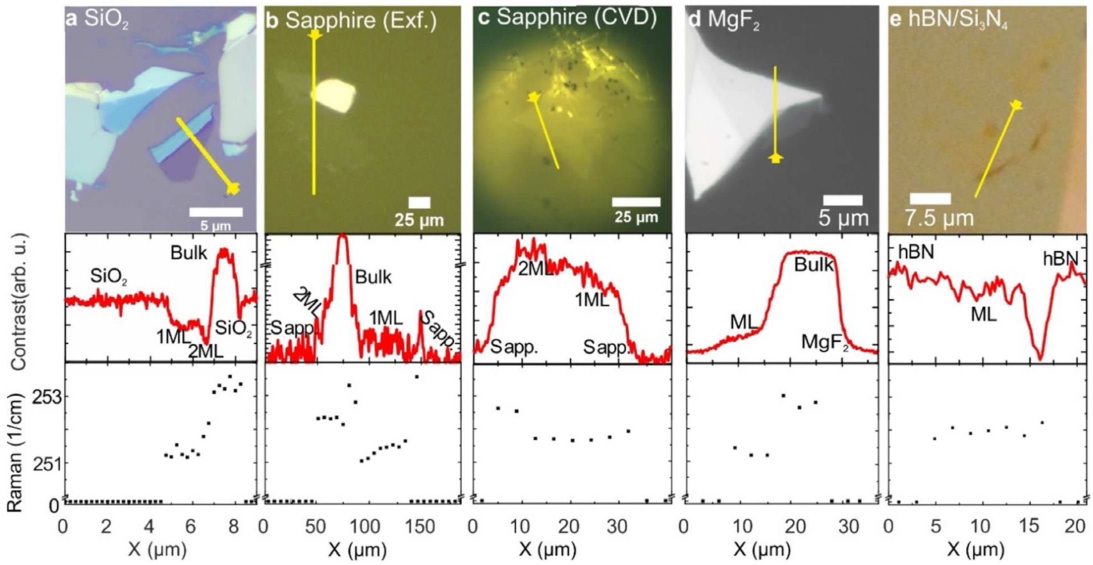

Figure 1. Microscopic images of the measured WSe_2 monolayers deposited on different substrates with cross sections. The substrates are (a) silicon dioxide, (b) sapphire exfoliated (exf.), (c) sapphire (CVD), (d) MgF_2, while in (e), a large flake of multilayer hBN is located underneath the WSe_2. Excluding (c), the investigated samples have been fabricated by mechanical exfoliation. The yellow line in each image indicates the path, along which the brightness cross-sections are taken and which are displayed in the respective charts in the lower row. Given the contrast variations, the layers can be identified and are marked in the cross sections. The lowest part of the figure shows the Raman peak position obtained along the yellow line. Wherever no WSe_2 peak is obtained, the graph shows zero.

TRPL measurements were conducted at 10 K and at 290 K under ultra-high vacuum conditions. During TRPL and μPL measurements, the laser spot size on the samples was approximately 4 μm. The time-averaged excitation densities at the pump spot delivered by the pulsed laser were determined to be 340, 1000, 2900, and 3400 W cm^{-2}.

The laser beam was focused under normal incidence onto the sample using a 20× microscope objective (NA 0.42). μPL emission from the sample was collected by the same objective. For spatial selection, an iris aperture in the real-space projection plane was used. In order to image samples, a CMOS camera in combination with optical lenses and mirrors is included. The μPL is collected by a grating spectrograph using a grating with 300 grooves mm^{-1} and an air-cooled intensified CCD, whereas for TRPL, an avalanche photo-diode (APD) is used with a time-correlated single-photon counting (TCSPC) unit. For TRPL measurements, the complete ML signal is acquired by the APD spectrally integrated behind a long-pass filter. For more details and explanations of the experimental methods, please see the methods section and supporting information.

Results and discussion

Photoluminescence spectra

Time-integrated μPL spectra at 290 K and 10 K have been acquired and are presented in figure 3. To investigate the power dependence of the μPL signal, four different excitation powers have been used. The excitation powers measured and verified before the beam splitter are 87 μW (blue), 250 μW (green), 720 μW (red) and 870 μW (black), corresponding to at maximum 43 μW, 125 μW, 360 μW and 430 μW after the beam splitter, which gives estimated mean pump densities of 340, 1000, 2900, and 3400 W cm^{-2}, respectively. To discriminate the contributing spectral components of the PL signal, a multi-peak evaluation with Gaussian peaks was performed. The sum of the Gaussian peaks is shown in light grey (which can be hardly distinguished from the emission spectra owing to the strong matching), while the single Gaussian peaks are shown in dark grey. The corresponding fit parameters *energy* (Peak position) and *line width (FWHM)* are summarized in the supporting information (see figure SI.4 and SI.5), while the

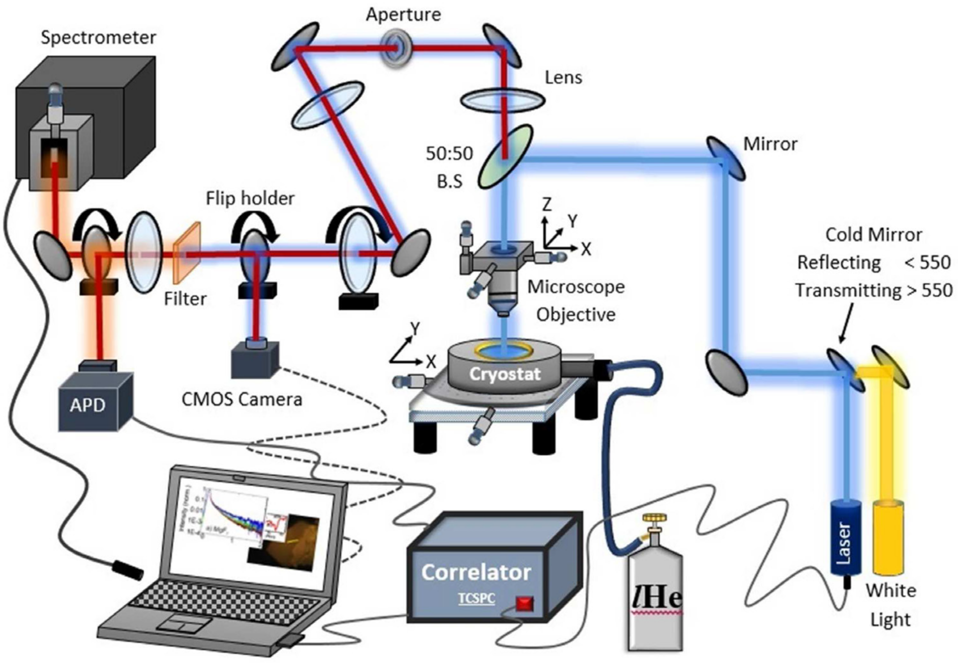

Figure 2. Schematic diagram of the micro-photoluminescence setup. The light of the Ti:Sa laser is focused onto the sample using a conventional confocal microscope setup. The setup with beam splitter (50:50 B.S.) uses a 20× objective to focus the light onto a 4 μm spot on the sample. The light is collected through the same objective. An iris aperture is used in the sample projection plane for spatial selection of the detection area. The sample can then be imaged using a removable lens and flip mirror in conjunction with a CMOS camera. The light can be focused onto the spectrometer slit for the acquisition of time-integrated spectra with an ICCD or onto an APD for transient μPL measurements, both at room temperature and at 10 K.

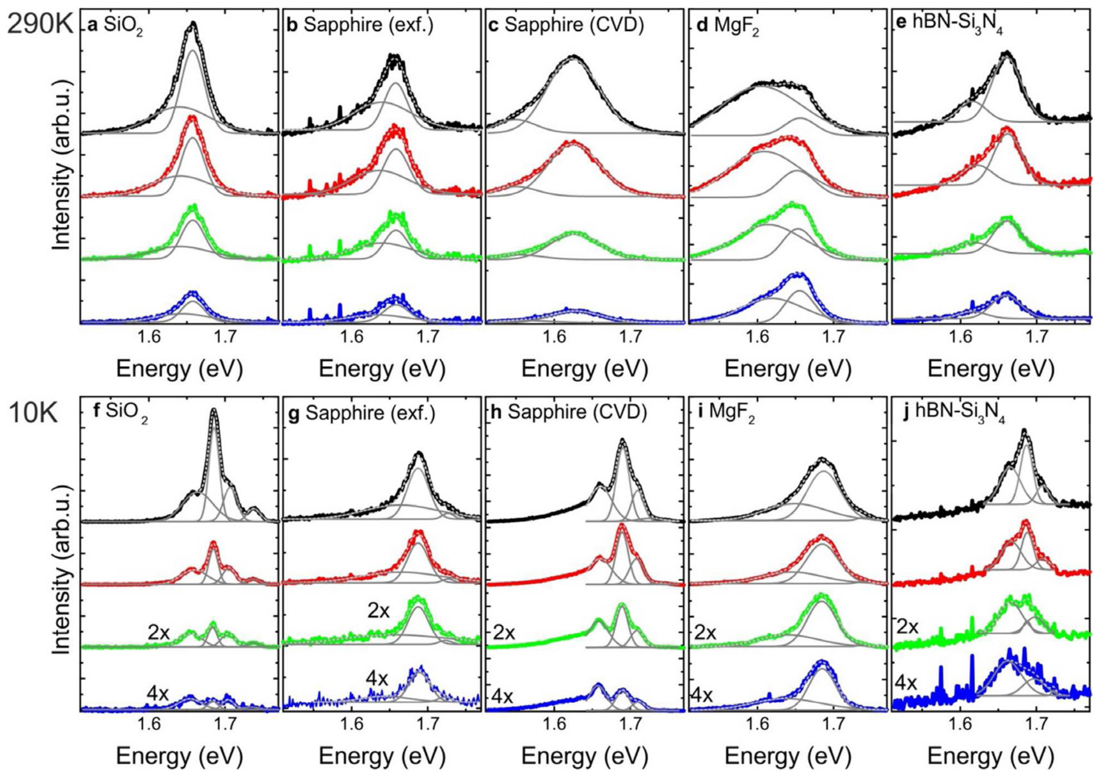

Figure 3. Time-integrated PL spectra of WSe_2 monolayers on different substrates at 290 K and 10 K for different excitation powers. The excitation densities shown are 340 (blue), 1000 (green), 2900 (red), and 3400 W cm^{-2} (black). The spectra have been fitted each with the sum of (at least) two Gaussian peaks (light grey dashed lines), with the underlying Gaussian peaks shown in dark grey. For better visibility, the spectra at 10 K for the lowest two powers have been scaled.

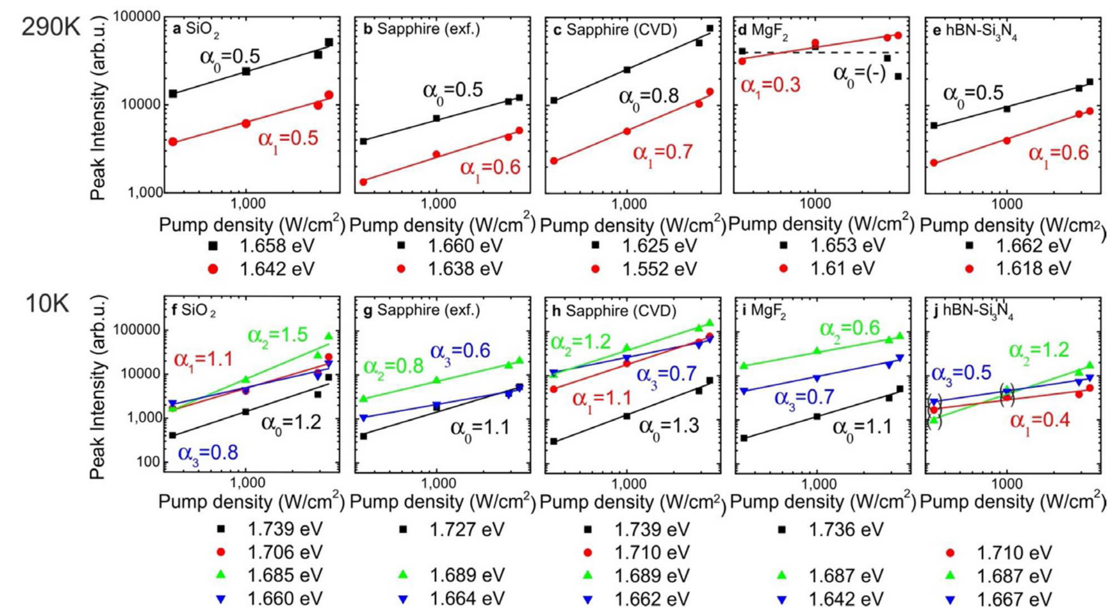

Figure 4. μPL intensity as a function of laser power for different substrates at 290 K and 10 K. The power dependence has been plotted on a double-logarithmic scale. The data series correspond to the Gaussian peaks used to fit the PL-spectra. The average peak energies resulting from multi-peak fitting is given in the legend. Furthermore, the series have been fitted to a power law (line) to get further insight into the recombination mechanism and for the sake of comparison. The four data series (symbols) summarized correspond to the features attributed to the exciton (black square), trion (red circle), biexciton (green up-triangle) and localized state (blue down-triangle) in the μPL spectra.

integrated peak intensities are discussed below (see figure 4).

At RT, a main peak and a red-shifted shoulder were observed for all substrates. Interestingly, the main peak attributed to the RT exciton is found at 1.66 eV for all substrates except for CVD-grown WSe_2 on sapphire (1.63 eV). The obtained excitonic energies for exfoliated samples are well comparable to Godde *et al* [68]. Nevertheless, the position of the exciton for the CVD-grown ML on sapphire is significantly different from that of bilayer emission and it agrees well with the result presented by Huang *et al* [22]. A spectral comparison of ML and bilayer emission is shown in the supporting information (see figure SI.3). Here, the particularly broad peak can be an indicator for a superposition of exciton and trion peaks, but can also hint at the mere occurrence of trions owing to a possibly larger rate of defect states (lattice dislocations, donor/acceptor states) as a possible consequence of CVD growth. Alternatively, one can understand the red shift of the exciton mode as a strain-induced effect owing to the hot temperatures in the furnace at which CVD growth takes place, while ML samples prepared by exfoliation at RT have very similar emission energies to one another. Since CVD ML are formed on the hot surface out of the vapor phase at elevated temperatures, the consecutive cooling after growth leads to tensions caused by the mismatch of the thermal expansion coefficients (TECs) of WSe_2 (in plane coefficient) TEC $= (1.1 \times 10^{-5}$/K–1.4×10^{-5}/K) [69, 70] and sapphire TEC $= (5 \times 10^{-6}$/K–8.3×10^{-6}/K) [71] at the relevant temperatures (300–900 K), which differ by a factor of 1.5–2. Qualitatively, the TEC of sapphire is less than that of WSe_2 over this temperature range. This leads to a scenario in which WSe_2 wants to shrink faster than the substrate during the cooling process but is stretched due to tension as a result of surface adhesion. Such conditions can indeed affect excitonic modes [38], as a stretched lattice with increased mean particle distances in the plane can exhibit a band gap energy reduction. This phenomenon has been confirmed during a high-temperature optical spectroscopy of ML WS_2 [72]. Here, the role of strain cannot be ruled out for the CVD-grown MLs of WSe_2 on sapphire (see supporting information), although it is claimed in [73] that strain may not be the reason for the difference between exfoliated and CVD-grown MoS_2 following a calculated small contribution of strain to spectral shifts.

Similar to [74, 75], we attribute the shoulder in the μPL spectra of our samples to trion emission. The peak center energies obtained from multi-peak fitting representing main and shoulder peaks are summarized in table 2 (see below). The data shown correspond to the averaged energies obtained for different excitation densities. Nevertheless, no significant peak shift has been found depending on the pump power. The errors correspond to the standard deviation of the values obtained at the four powers.

Interestingly, a subtle correlation between the refractive index of the substrate and the energetic position of the RT exciton modes can be observed (see table 2), although the refractive index was only changed for the half space, i.e. on one side of the sample. However, the details of such dependency cannot be clarified within the scope of this work. Nevertheless, it is expected that the influence of a dielectric medium

Table 2. Calculated energy values for exciton, trion, biexciton and bound states at 10 K and 290 K in WSe_2 MLs deposited on different substrates. Energies are rounded to three decimal figures for the sake of legibility. The provided errors with three decimal figures correspond to the standard deviation of the values obtained for the four pump-power settings. The values of the exponent factor are also indicated in the respective row and column. Results shown in parentheses cannot be attributed to the respective species.

T (K)	Feature	SiO_2/Si	Sapphire	Sapph. (CVD)	MgF_2	hBN/Si_3N_4
290	Exciton (eV)/	1.658 ± 0.001	1.660 ± 0.001	1.625 ± 0.002	1.653 ± 0.002	1.662 ± 0.001
	α-value	0.5	0.5	0.8	(−)	0.5
290	Trion (eV)/	1.642 ± 0.002	1.636 ± 0.003	1.552 ± 0.004	1.610 ± 0.045	1.618 ± 0.005
	α-value	0.5	0.6	0.7	0.3	0.6
10	Exciton (eV)/	1.739 ± 0.002	1.727 ± 0.002	1.739 ± 0.013	1.736 ± 0.003	
	α-value	1.2	1.1	1.3	1.1	
10	Trion (eV)	1.706 ± 0.001		1.710 ± 0.001		1.705 ± 0.010
	α-value	1.1		1.1		(0.4)
10	Biexciton (eV)/	1.685 ± 0.001		1.689 ± 0.001		1.687 ± 0.005
	α-value	1.5		1.2		1.2
10	Feature (eV)/		(1.689 ± 0.001)		(1.687 ± 0.002)	
	α-value		(0.8)		(0.6)	
10	Localised state (eV)/	1.660 ± 0.005	1.664 ± 0.016	1.662 ± 0.004	1.642 ± 0.005	1.667 ± 0.002
	α-value	0.8	0.6	0.7	0.7	0.5

change for MLs on the optical dipoles of MLs is noticeable even when one half space remains at $n = 1$, since the field lines of such Rydberg-like dipoles penetrate into the MLs surrounding environment (as described by the literature, see [76]). In the meanwhile, during preparation of this article, different studies have been concluded and are now available to the community of researchers interested in the field of 2D materials that shed light on the influence of the dielectric environment on the ML signatures by means of different approaches and techniques, which may be briefly discussed and summarized here.

To address the influence of the dielectric environment on the ML emission, [75] presents a comparative room-temperature study which involves various liquids with different refractive index as cover layer for the MoS_2 ML on SiO_2/Si. It is demonstrated experimentally that the binding energy decreases with increasing dielectric constant, for both A and B exciton, and A trion, the binding energy of which is about one order of magnitude smaller than for the uncharged exciton [75]. Furthermore, the measured intensity ratio between A trion and A exciton is changing as a function of the dielectric environment. In addition, the overall intensity increases with increasing dielectric constant.

In other studies, it has been shown that, although surrounded by vacuum from both sides, suspended MLs seemingly do not show a significant wavelength shift due to a change of the dielectric function of the environment [55], which is attributed to band gap renormalization simultaneous to the change of binding energy. This is also stated in [54]. Starting from the changing trion and exciton intensities, the authors argue that there are two types of doping. Either it can be attributed to water that is capped between the substrate and the ML or by the substate itself. For the case of WSe_2 studied here, the latter effect is said to be the dominant one. According to [54], in contrast to the MoS_2 and WS_2 flake studied in that work, WSe_2 has been found to be intrinsically p-doped, concluding that if it is grown on an n-doped substrate, the radiative recombination is amplified.

The work presented in [77] discusses the use of high pulsed magnetic fields to induce a diamagnetic shift of the ML WSe_2 resonance using samples with three different environmental settings. From the diamagnetic shift, the exciton radius is directly deduced, which shows an increase with increasing dielectric constant of the environment. At the same time, the exciton binding energy increases.

In the present work, the lowest refractive index material, MgF_2, has the lowest exciton energy while the highest refractive index substrate (see table 1), hBN/Si_3N_4, features the highest, with a total difference of about 9 meV in peak positions (see table 2). Nevertheless, there is no unambiguous correlation with the refractive index of the substrate material. For example, this correlation has not been found for the emission attributed to the trion, and also not for the features measured at 10 K. The observation of a trend at RT also excludes the CVD-grown ML on sapphire because of its strong peak shift. This deviation of the CVD result at RT can be explained by the ML fabrication technique; CVD ML fabrication takes place at high temperatures and can introduce strain to both the substrate surface and the deposited material as a result of the annealing process and subsequent cooling. Moreover, it is expected that the incorporation of defects and impurities into the 2D lattice is stronger for CVD grown MLs than for exfoliated crystals, suggesting a broader spectral distribution of RT emission and more emission from defects for CVD MLs.

In sum, it seems that the substrate only slightly affects the μPL features of WSe_2 at RT (see fit parameters summarized in the supporting information, figures SI.4 and SI.5). This may increase the importance of WSe_2 as a 2D material due to its ability to be deposited on a variety of substrates without losing its general spectroscopic attributes.

In contrast to the RT case, at $T = 10$ K four different PL emission features were identified for ML WSe_2 isolated on SiO_2 and sapphire (CVD), whereas only three peaks were observed for WSe_2 exfoliated on sapphire (exf.), hBN/Si_3N_4 and MgF_2 substrates. The four peaks can be identified as exciton (1.73 eV), trion (1.71 eV), biexciton (1.69 eV) and localised states (1.66 eV and below) and show good agreement with the energetic positions found in [38, 49, 68]. Table 2 summarizes the results of figures 3(a)–(j).

In general, the energetic positions of all features are comparable within the fit accuracy for all substrates except for the CVD grown sample. Therefore no trend can be seen as a function of the refractive index. For some samples, no distinct exciton and trion features were obtained, and a significant separation of such two species was not found. Consequently, the higher energy shoulder peak(s) (even if two species could be presumed) was fitted with one Gaussian peak. The exfoliated MLs on sapphire and MgF_2 clearly show broader central peaks (FWHM ~25–40 meV) compared to the other samples (FWHM ~15 meV) (for more details see the supporting information). This could be an indicator of different surface qualities or differences with respect to defect states and impurities. Nevertheless, the values obtained for excitonic features are in good agreement with those reported by Wang *et al* [40] (exciton: 10 meV, trion: 15 meV) and exhibit quite narrow line widths and comparable energy positions within the batch of different samples. Here, spectral similarities are very pronounced, while no trend in relation to the refractive index is evidenced. However, this can be understood as many factors can influence the spectral properties, such as strain effects in low-temperature ML-substrate compounds and the compensation of opposing effects such as binding energy modifications and gap renormalization, which cannot be quantified readily in such a study.

Relationship between laser power and μPL intensity

To get further insight into the recombination processes, double-logarithmic plots of the power dependence (P_L) of each peak's intensity (I_{PL}) are presented in figure 4. This type of analysis technique is useful since the emission of localized states [68] or bound states [49] grow more slowly than exciton emission with increasing pump power and exhibit sub-linear power dependence. Consequently, using P_L–I_{PL} measurements, excitonic features can be identified by their super-linear behavior [49].

All the logarithmic plots in figures 4(a)–(j) can be described by the power law-equation, i.e. $I_{PL} \propto P_L^{\alpha}$ [49], where α is the linearity or exponent factor. The corresponding peaks' center energies resulting from the fits are given in the legends and are summarised in the supporting information. The up-to-four data series (solid symbols) correspond to the up-to-four distinct features attributed to the exciton (black square), trion (red circle), biexciton (green up-triangle) and localized state (blue down-triangle) in the μPL spectra of the different samples.

For the RT measurements of WSe_2 on SiO_2, WSe_2 exfoliated on sapphire and WSe_2 on hBN/Si_3N_4, we found values for α close to 0.5. While for CVD-grown WSe_2 on sapphire and MgF_2, another behavior is observed. Referring to the rate equations describing the recombination of free and localized carriers, 0.5 corresponds to the recombination of electron–hole pairs at localized centers [78]. The slightly larger values for CVD-grown WSe_2 on sapphire can be explained by the presence of defects [74]. For MgF_2 it seems that for higher powers, the excitonic emission vanishes after a period of intensity saturation while the trion emission increases predominantly. Here, no α factor can be extracted for the higher-energy feature, as the behavior is governed by a different effect which can be attributed to differences in the surface quality and flake quality and which give preferably rise to the side feature. Similar to [54, 75] the intensity ratio between exciton and trion changes with the substrate.

For LT measurements, the observed linearity factors show a different behavior in comparison to the ones obtained at RT. The α -value for the exciton lies between 1.1 and 1.3 which is comparable to the values given in [74] and within the theoretical expectation given by [78]. For the trion, we obtain values of 1.1. These are comparable to earlier reported values from Yan *et al* [39]. A possible reason for the smaller α-value of the trion for WSe_2 on hBN/Si_3N_4 might be related to the obtained background PL signal of Si_3N_4 which reduced the quality of the peak fitting at low excitation densities. Indeed, at higher pump densities, the slope recovers from the negative effect of background PL. The values of the superlinearity on SiO_2/Si, Sapphire (CVD) and hBN/Si_3N_4 for the biexciton (1.2–1.5) match the expected higher value of 1.5 reported earlier [49]. Although the other two samples exhibit an emission at the same energetic position as the biexciton, the value for α and the line width of the peak do not match the expected value. As discussed earlier, these samples probably inherit more defects leading to more localized emission. Unsurprisingly, the localized states show an α-value strongly below 1 and match the expected value of 0.5 [68]. A summary of all experimentally determined α factors is given in table 2.

To verify the excitonic character of the features in analogy to [49], measurements with circular-polarized light with excitation-detection configurations $\sigma^+ \rightarrow \sigma^+$ and $\sigma^+ \rightarrow \sigma^-$, respectively, have been performed with both continuous-wave (cw) excitation (at 1 kW cm^{-2}, which is below the experienced cw-damage threshold) and pulsed excitation (as used for all μPL and time-resolved PL in this work). Since pulsed pumping exhibits high (peak) excitation densities, it gives rise to the formation of biexcitons, which can be then clearly observed in our polarization-dependent measurements. In order to obtain a reasonable signal for all samples, the average pump-power density is set to 10 kW cm^{-2} (which is close to the experienced damage threshold). According to previous studies, defect states exhibit a degree of circular polarization $|\rho| < 0.1$, while excitonic states show $|\rho| > 0.1$ [49]. The degree of circular polarization is defined as:

$$\rho = \frac{I(\sigma^+) - I(\sigma^-)}{I(\sigma^+) + I(\sigma^-)} \tag{1}$$

where $\sigma^\pm$ defines the detected polarization state. Correspondingly, for the features attributed to exciton (X), trion (X^*) and biexciton (XX) states, a significant circular polarization degree is obtained while the defect states basically remain unchanged in detected intensity for the different circular-polarization configurations, as can be exemplarily seen in figure 5 for CVD-grown ML WSe_2 on sapphire.

Owing to its more density-dependent formation probability compared to excitons and charged excitons, emission from the biexciton state is only observed for pulsed excitation at elevated pump rates, while the exciton, trion and defect emission are found for both cw and pulsed excitation. The respective degrees of circular polarization obtained from this measurement can be found summarized in table 3 (for polarization-dependent spectra, see supporting information, figure SI.6). This study clearly reveals the excitonic nature of various features recorded at 10 K in agreement with the findings from the intensity-dependent considerations, and particularly confirms the excitation of biexcitons in the considered ML systems. Here, the average power for cw and pulsed excitation are 1 kW cm^{-2} and 10 kW cm^{-2}, respectively, whereas these measurements were performed separately with regards to the μPL-TRPL measurements. Values in parentheses do not exhibit the expected magnitudes for the corresponding species.

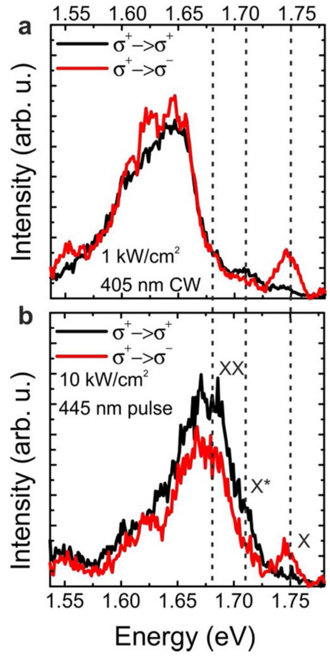

Figure 5. μPL spectra of co- and cross-polarized signal for ML WSe_2 on sapphire (CVD) at 10 K. (a) μPL recorded for circular-polarized continuous-wave excitation with same circular polarization (black) and opposite polarization (red). (b) μPL spectra for the same two circular polarization configurations for circular-polarized pulsed excitation. The emission energies for excitons (X), trions (X^*) and biexcitons (XX) are marked by dashed lines.

Time resolved photoluminescence (TRPL)

In figure 6 a bar chart of the different decay times for all five substrates is shown. Triexponential fits were used to systematically extract the first (fast) and second (slow) decay time from each curve (an example is shown as an inset in figure 6 and others can be found in the supporting information, together with the fit equation and an overview on the fit parameters, including first, second and third time constants and their amplitudes, respectively). The triexponential fits were used for all data; although for some data biexponential fits would have been enough (that would lead the extracted third time to be very similar to the second time). This was done to maintain comparability. While the third time is not used for comparison as explained in the supporting information, it can be found in the summary of parameters in table SI.1. The corresponding bar chart in figure 6 shows the fast time constant (τ_1) and the slow time constant (τ_2) in comparison to each other at 290 and 10 K for all measured samples. In the following, we describe our results in a qualitative and not quantitative manner, given the fact that the fast times in the range of a few tens of ps do not represent real decay times, since the temporal resolution of our setup is around 40–50 ps. Since no post-processing, such as reconvolution or deconvolution, was performed, all TRPL (substrate-dependent and power-dependent) results remain totally comparable and allow one to extract trends within the uncertainty range of a few ps (of the exponential fitting) at very short time scales.

For all the substrates measured, τ_1 and τ_2 seem to be more pump-density-independent at $T = 290$ K than at $T = 10$ K. This can be explained by noting that biexcitons, which have a higher time constant, are the most density-dependent feature [49]. There are no biexcitons available at $T = 290$ K as shown earlier in figure 3 and table 2. At RT, WSe_2 on SiO_2/Si and on MgF_2 show longer decay times than the other samples. Additional shortening of the fast decay time is observed as a function of the excitation density. Similarly to Mouri *et al* [79], we attribute this to higher exciton–exciton annihilation. Due to the higher pump rates, the necessary diffusion length for exciton–exciton annihilation shrinks. The slow decay time τ_2 shows the same behavior as the fast decay time. Again, the slow decay times for SiO_2/Si and MgF_2 are longer than the slow decay times for the other substrates. The slow decay times for sapphire (exf.), MgF_2 and SiO_2/Si get faster with higher excitation powers while the slow decay times for the other two

Table 3. Degree of circular polarization for pulsed and cw excitation. The extracted polarization degrees for different species identified in μPL spectra at 10 K are summarized for both pulsed and cw excitation of ML WSe_2.

Pol. degree ρ	SiO_2/Si		Sapphire		Sapph. (CVD)		MgF_2		hBN/Si_3N_4	
Pump:	Pulse	cw	Pulse	cw	Pulse	cw	Pulse	cw	Pulse	cw
Exciton	0.19	(0.02)	0.27	0.12	0.44	0.64	0.27	0.19		
Trion	0.42		0.25	0.27	0.30	0.21			(0.06)	0.24
Biexciton	0.37				0.24				(0.03)	
Feature			0.21	0.29						
Localised state	0.02	(0.16)	(0.13)	(0.20)	0.08	0.03	0.08	0.03	0.03	(0.29)

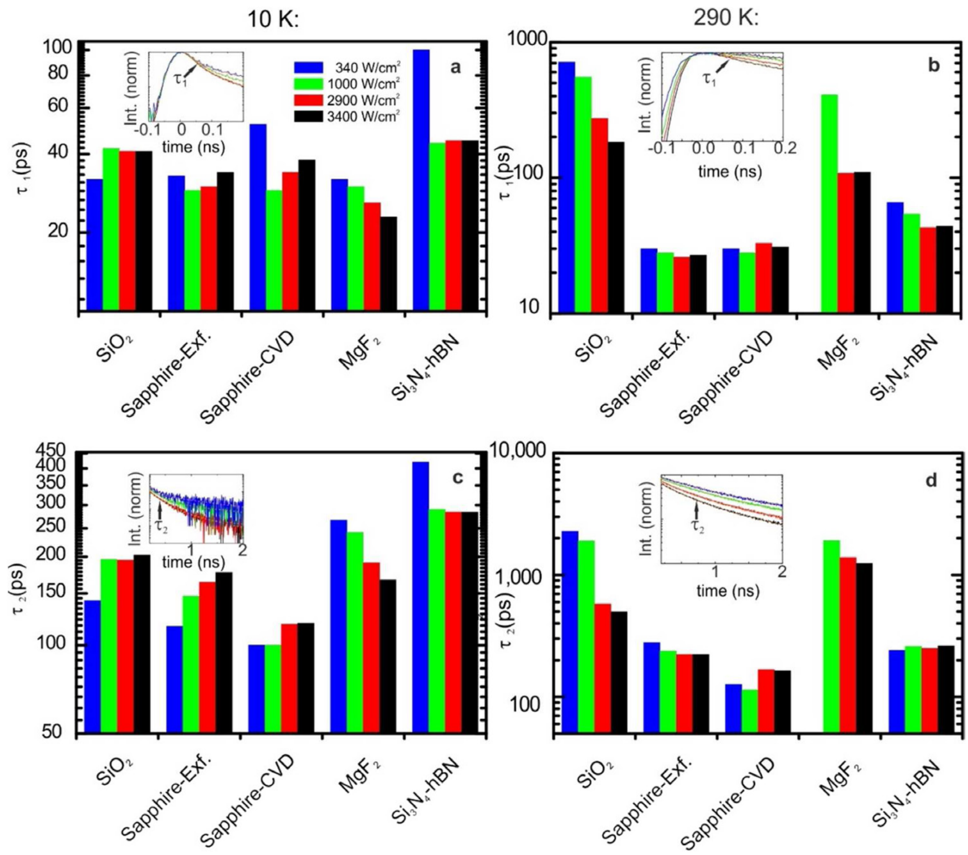

Figure 6. Comparison of time constants derived from transient PL of WSE_2 monolayers on different substrates at different powers. The temperature for (a) and (c) is 10 K and for (b) and (d) is 290 K. The inset in each histogram is an exemplary TRPL plot for WSe_2 on SiO_2 from which the values of time constant are extracted using triexponential fitting. The overview on all transients is given in figures SI.7 and SI.8.

samples remain constant. This increase in decay rates is again attributed to exciton–exciton annihilation. At RT, changes to the temporal characteristics can not only be attributed to the substrate materials properties but also to other effects like interactions with phonons and Auger processes.

To verify the observation of exciton–exciton annihilation, the transient μPL obtained at RT have been fitted with a bimolecular function. Therefore, the following differential equation for the exciton population N describing the decay including the annihilation is used [80]:

$$\frac{\mathrm{d}N}{\mathrm{d}t} = G(t) - \frac{N}{\tau} - \beta N^2 - \gamma \frac{N^2}{\tau^{\mathrm{d}}} \qquad (2)$$

in which the first term describes the exciton generation term by the fs-pulsed source, where α is the unsaturated absorption coefficient, P the excitation pulse energy, λ the excitation wavelength, r the radius of the excitation spot, N_{gr} the initial density of ground states and σ_{t} the temporal width of the pulsed laser:

$$G(t) = \frac{\alpha P \lambda}{2\pi r^2 hc} \frac{N_{\mathrm{gr}} - S(t)}{N_{\mathrm{gr}}} \frac{\exp\left(-\frac{(t-t_0)^2}{2\sigma_{\mathrm{t}}^2}\right)}{\sqrt{2\pi\sigma_{\mathrm{t}}^2}}, \qquad (3)$$

with

$$S(t + \mathrm{d}t) = G(t)\mathrm{d}t. \qquad (4)$$

The second term of equation (2) describes the radiative decay of excitons with time constant τ that has been

Table 4. Fit parameters of the bimolecular function for the different samples used to model RT transient μPL.

Parameters	SiO_2	Sapphire	Sapph. (CVD)	MgF_2	hBN/Si_3N_4
β (cm^2 fs^{-1})	$2.6 \times 10^{-16} \pm 0.2 \times 10^{-16}$	$1.1 \times 10^{-17} \pm 0.2 \times 10^{-17}$	$1.5 \times 10^{-16} \pm 0.2 \times 10^{-16}$	$1.8 \times 10^{-17} \pm 0.2 \times 10^{-17}$	$1.1 \times 10^{-16} \pm 0.2 \times 10^{-16}$
γ (cm^3 10^{-13} s^{d-1})	$2 \times 10^{-17} \pm 0.2 \times 10^{-17}$	$4 \times 10^{-18} \pm 0.2 \times 10^{-18}$	$4 \times 10^{-18} \pm 0.2 \times 10^{-18}$	$2 \times 10^{-18} \pm 0.2 \times 10^{-18}$	$5 \times 10^{-18} \pm 0.2 \times 10^{-18}$
d	0.19 ± 0.02	0.17 ± 0.02	0.20 ± 0.02	0.19 ± 0.02	0.04 ± 0.02
τ (ps)	210 ± 5	41 ± 2	55 ± 2	418 ± 10	116 ± 5

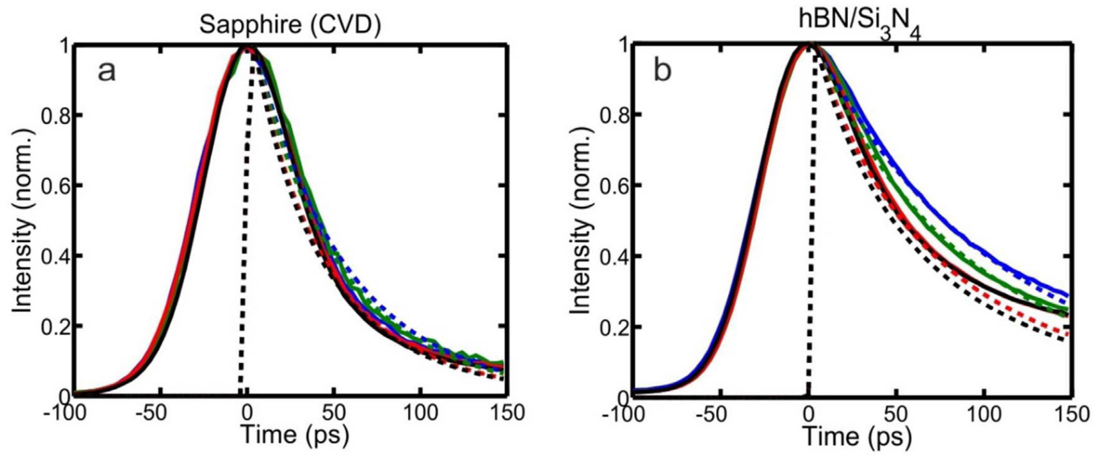

Figure 7. Representative transient μPL of WSe_2 at 290 K with bimolecular fit function. (a) A weak power-dependent shortening of the PL decay for CVD-grown WSe_2 on sapphire is shown in comparison to (b) a more pronounced shortening in the case of WSe_2 on hBN/Si_3N_4. The experimental data is shown as lines while the modeled data obtained from a bimolecular fit function is shown as dotted lines. For the given excitation densities of 340 (blue), 1000 (green), 2900 (red) and 3400 W cm^{-2} (black), respectively, a shortening of the decay with increasing excitation densities can be well explained by exciton–exciton annihilation, as the rate-equation-based fit function after [79] can reproduce the observed trends correctly.

extracted from the μPL transient obtained at lowest fluence. The last two terms of equation (2) describe the collisional bimolecular annihilation and the long-range time-dependent bimolecular annihilation, respectively. β denotes the diffusion-limited bimolecular annihilation rate, while γ denotes the long-range annihilation rate. d is a constant that is given by the dimensionality and the disorder in the system and has been considered a fit parameter.

This model describes the power-dependent trend of the normalized transients well, as an exemplary fit to experimental data shows in figure 7. The fitted RT transients of the MLs on other substrates are provided in the supporting information, while the resulting fit parameters (with an assumed certainty range corresponding to reasonable deviation from best-fit parameters) for all samples are shown in table 4.

The extracted annihilation rates are similar to the ones derived by Yu *et al* [82], Mouri *et al* [79]. For a practical device, MLs on substrates with small annihilation rates can be used at high pump rates until exciton–exciton annihilation becomes dominant [82].

At 10 K, the fast decay time at very low pump-densities decreases with increasing power, while at higher pump densities, the decay time remains nearly the same or seemingly increases. A comparison with the power dependence of the different species in the spectrum (figure 4) shows that at the lowest power trion, biexciton and localised state emissions equally contribute to the total emission (in the spectrally integrated detection scheme).The exciton does not play a pronounced role. At medium power the fraction of the localised states' emission intensity with respect to the total emission is reduced. At high excitation densities the emission from biexcitons dominates the signal [49].

At LT, the substrates become more important as phonon and Auger processes become negligible. Therefore, we revisit the relationship between refractive index and emission properties. Here, a correlation between the refractive index and the general behavior of the fast decay time is indicated. The decay times of the lowest-refractive-index substrate appears to be the fastest while the one for the highest-refractive-index substrate exhibits the slowest decay times. However, this could also reflect the quality of the surface, which at LT could be the significant factor for the exciton dynamics. This reasoning explains the slower decay in the WSe_2–hBN/Si_3N_4 case, where hBN provides an atomically smooth surface for the ML. Simultaneously, spectral properties do not exhibit better excitonic features for this ML-substrate combination, which supports the claim that a non-negligible effect of the dielectric surrounding could be the reason for the fast time constant's trend.

The slow decay times at LT displays two trends. MgF_2 and hBN/Si_3N_4 exhibit faster decay times with higher pump densities, while the other substrates' decay times slow down slightly with increasing densities. While MgF_2 and hBN/Si_3N_4 can be fitted with only two time constants, the other samples need to be fitted with three time constants. Nevertheless, all samples have been fitted with three times for better comparability.

All TRPL fit parameters are listed in table SI.1 of the supporting information. Additionally, figure SI.11 in the supporting information summarizes decay times extracted from the TRPL data using a single-exponential fit to the respective data in the range of the second time constant, which is not affected by our setup's resolution and shows similar trends as discussed above.

Conclusions

We have studied μPL and TRPL from WSe_2 deposited on different substrates at both RT (290 K) and cryogenic temperature (10 K). Spectral components such as excitons, trions, biexcitons, and bound states have been identified and compared for different substrates. At RT, a small energy shift of the excitonic mode correlating with the refractive index change of the substrate material is indicated. At LT, all ML samples exhibit remarkably similar peak energies for the different species obtained in their emission spectrum. Interestingly, the emission properties of CVD-grown WSe_2 on sapphire are very comparable to other ML-substrate cases at LT, while at RT, in contrast to exfoliated WSe_2 on the same material, its emission shows a pronounced red shift of modes, which can be attributed to strain as a consequence of the hot growth process. The relatively high values of the exponent factors α for WSe_2/SiO_2, WSe_2/sapphire (exf.), and WSe_2/sapphire (CVD) at 10 K may reflect the dominance of corresponding excitons, trions, and biexcitons among other features in WSe_2 PL at cryogenic temperatures, as further suggested by polarization-dependent measurements revealing particularly the biexciton state among those. Measured fast and slow decay times of the ML emission, τ_1 and τ_2 at 290 K indicate a power-dependent increase of the decay rate which is attributed to exciton–exciton annihilation. Whereas at 10 K, the pronounced emergence of excitonic features determines the decay trends with a subtle indication that the refractive index of the dielectric environment may have an effect on the fast decay rates. Thus, this study inspires further detailed investigations concerning substrate-related optical properties of 2D materials and supports the tailoring of application oriented ML systems.

Methods

Sample preparation

Exfoliation in the group in Marburg: All WSe_2 samples are prepared by mechanical exfoliation using bulk WSe_2 crystals (*Manchester Nanomaterials*). We exfoliated bulk crystals (*Scotch Magic 3M*) and then transferred them onto a transparent viscoelastic substrate (*Gel-Pak gel film PF-30-X4*). MLs were then identified by optical contrast using a bright field microscope and transferred onto substrates using the viscoelastic dry-stamping method [81]. All substrates were cleaned in an ultrasonic bath with acetone (99.9% purity) and then rinsed with methanol. WSe_2 on SiO_2/Si samples were fabricated using a 300 nm thermal oxide layer substrate (*IDB Technologies, Ltd*). WSe_2 on h-BN/Si_3N_4 were fabricated by transferring multilayer h-BN (*Manchester Nanomaterials*) onto a 75 nm silicon nitride layer on silicon (*IDB Technologies, Ltd*). WSe_2 on MgF_2 (*Shanghai OEMC Co., Ltd*) was fabricated using the same technique. After transfer, samples were measured as is and no post processing was applied. All samples were continuously stored in vacuum.

Exfoliation in the group at the Columbia University: Samples were exfoliated onto SiO_2/Si (290 nm) and sapphire using an established scotch tape mechanical exfoliation method (using *Scotch Magic 3M*). A heated exfoliation was used for TMDC crystals following this, after [83] to increase the size of the MLs.

CVD growth of WSe_2 ML on a sapphire substrate: The sample was comprised of a tungsten source carrier chip (5 nm WO_3 thin film on 90 nm SiO_2) and a sapphire substrate (*Ted Pella, Inc.*). Tungsten oxide (WO_3, 99.99%, *Kurt J. Lesker*) was deposited on SiO_2 via electron beam evaporation. The tungsten source chip was covered, in face-to-face contact, by the sapphire substrate as the growth substrate. The sample was loaded into the center of a 2″ diameter and 24″ long quartz tube (*MTI Corp.*), and a ceramic boat with 1 g of selenium powder (99.99%, *Sigma-Aldrich*) was located upstream in the quartz tube. After loading, the ambient gas of the tube was purged out via mechanical pump to the base pressure of 10 mTorr. The furnace was heated to 750 °C at a 13 °C min^{-1} ramping rate and the temperature held at 750 °C for 4 min, then it was raised to 850 °C at 13 °C min^{-1}. 20 sccm of Ar gas (5.0 UH purity, *Praxair*) was introduced at 500 °C (increasing temperature) to reduce moisture inside of the tube and closed at 500 °C (decreasing temperature). Hydrogen (15 sccm, 5.0 UH purity, *Praxair*) gas was supplied to improve WO_3 reduction from 700 °C (increasing temperature) to 600 °C (decreasing temperature). The growth pressure was 1.6 Torr. After 20 min at 850 °C, the furnace was cooled down to RT naturally.

Experimental setup

μPL: The sample was mounted in a helium-flow cryostat in the μPL setup. All data shown are time-integrated spectra. For excitation, a pulsed titanium-sapphire laser (*SpectraPhysics Tsunami*) with a tuneable emission wavelength of 700–1000 nm, a pulse duration of 100 fs and a repetition rate of 80 MHz was used. The light from the laser was frequency doubled by nonlinear optics (*CSK Optronics Super Tripler 8315*) to provide an excitation wavelength of 445 nm. For detection, a gated intensified charge-coupled device (ICCD) in shutter mode behind a monochromator (*Princeton Instruments Acton SP2300*) was used, using full chip exposure (2D chip read out) and manual integration and truncating of the exposed CCD area. Identification of ML positions was performed using extracted integrated spectra which show distinct emission features of MLs. The image of the sample is focused onto the monochromator entrance slit for spectroscopy. The power-dependent μPL measurements are conducted at 10 K and at 290 K under ultra-high vacuum (~10^{-6} mbar) conditions using a cooling system with liquid helium. Pump-power-dependent measurements were performed at same average power levels, carefully set prior to each measurement run. The investigated powers were set by a neutral density filter wheel (discrete steps). The relevant power levels were sequentially changed after the accomplishment of a spectral measurement and its corresponding time-trace measurement. Detection of the μPL signal from the sample takes place behind a spatially filtering aperture in a confocal microscopy geometry. Two long-pass filters were used that block laser light below 650 nm. For evaluation, the recorded 2D spectra (x axis: wavelength, y axis: pixel corresponding to location) is integrated vertically over the relevant pixels corresponding to the excitation spot, minimizing noise and contribution from camera artifacts. The same procedure has been applied to all spectra, integrating over the same amount of pixels. The signal was recorded after optimizing the microscope objective's focus for the most focused projection onto the ICCD (i.e. monochromator entrance slit). With the magnification of the 20× microscope objective and 200 mm focus length of the projection lenses, a reasonable magnification is obtained.

To perform circular polarization measurements a λ/4-plate was inserted into the exciting laser beam. Another λ/4-plate together with a linear polarizer was used for detection of the photoluminescence. For the only case of cw excitation in this work which was used for the polarization dependent measurements, a cw laser with 405 nm was used.

TRPL: Here, highly sensitive fast single-photon counting modules (SPCMs) with timing resolution down to <50 ps (*MPD, PDM Series, Single Photon Avalanche Diodes, 100 μm active area*) were used, providing maximum flexibility regarding photon fluxes. The drawback of high count rates is the temporal resolution of the detector. To obtain maximum temporal resolution, a stand-alone time-correlated single photon counting (TCSPC) unit with 4 ps histogram time resolution (minimum binning of the *PicoQuant PicoHarp 300*) was employed. Given the instrument response function of the device with decay time between 40 and 50 ps (probed by exposure of the excitation laser), time constants shorter than 40 ps are not considered reliable, even if trends are still seen towards shorter times. No reconvolution or deconvolution has been applied to provide experimental time constants as is, extracted from triexponential fit curves. This is understandable as the measured instrument response using substrate-back-reflected laser light at 445 nm and differing count rates shows a decay of 48 ps that is slightly slower than the fastest measured sample life times (measured above 700 nm). The detection of the signal from the sample in the μPL setup is similar to μPL spectroscopy, however before the monochromator (using a flip mirror to divert the beam onto the SPCM). Coarse spectral filtering is achieved by long-pass filters, which sufficiently suppress back-scattered laser light and substrate background PL below 650 nm. Before a TRPL measurement is started, ML PL is confirmed for the pumped and detected region by time-integrated spectra. No other species than the ML PL was detected by the spectrometer for the long-pass filtered signal. Only the Si_3N_4 substrate featured a broad background spanning the range of 660–820 nm. The Si_3N_4 PL background was drastically reduced when an hBN buffer layer was employed. This broad background was brighter than any low-temperature ML signal in case of WSe_2 on pure Si_3N_4, which forced us to disregard low-temperature PL from WSe_2 on Si_3N_4. No particular background subtraction has been applied to the spectra other than noise background subtraction, as can be seen in hBN-Si_3N_4 spectra. Room-temperature measurements for different sample positions (and flakes) on the same substrate material confirmed strong similarities and reproducibility of emission properties.

Acknowledgments

The authors acknowledge financial support by the Philipps-Universität Marburg, the German Research Foundation (DFG: SFB1083) and the German Academic Exchange Service (DAAD). Work at Columbia was funded by the NSF MRSEC under DMR-1420634. AR-I thanks Tony Heinz, Alexey Chernikov, Özgür Burak Aslan for invaluable discussions on 2D materials and properties, and Tineke Stroucken as well as Martin Koch for helpful discussions on excitonic features.

Author contributions

AR-I initiated and guided the joint work on substrate-dependent optical properties of 2D materials in Marburg with the help of YDK, EHY and JH Different sample types were envisioned and fabricated by DR, DA, KK under supervision of YDK, EHY, JH and AR-I The optical setup was established by DR, MH, OAM, KH, SEB and AR-I The experiments were designed and conducted by SL, LMS, DR, JK, MH, OAM, XL, WH and AR-I and the results discussed with the support of all coauthors. The manuscript was written by SL, LMS, KH, SEB and AR-I with input from all co-authors. SL and LMS contributed equally to this work.

Author information

The authors declare no competing financial interests.

References

[1] Wang Q H, Kalantar-Zadeh K, Kis A, Coleman J N and Strano M S 2012 Electronics and optoelectronics of two-dimensional transition metal dichalcogenides *Nat. Nanotechnol.* **7** 699–712

[2] Lu J, Liu H, Tok E S and Sow C 2016 Interactions between lasers and two-dimensional transition metal dichalcogenides *Chem. Soc. Rev.* **45** 2494
[3] Choi M S *et al* 2014 Lateral MoS_2 *p–n* junction formed by chemical doping for use in high-performance optoelectronics *ACS Nano* **8** 9332–40
[4] Yang W *et al* 2016 Electrically tunable valley-light emitting diode (vLED) based on CVD-grown monolayer WS_2 *Nano Lett.* **16** 1560–7
[5] Zibouche N, Philipsen P, Kuc A and Heine T 2014 Transition-metal dichalcogenide bilayers: switching materials for spintronic and valleytronic applications *Phys. Rev.* B **90** 125440
[6] Perera M M *et al* 2013 Carrier mobility in few-layer MoS_2 field-effect transistors with ionic-liquid gating *ASC Nano* **7** 4449–58
[7] Li H, Wu J, Yin Z and Zhang H 2014 Preparation and applications of mechanically exfoliated single-layer and multilayer MoS_2 and WSe_2 nanosheets *Acc. Chem. Res.* **47** 1067–75
[8] Das S, Dubey M and Roelofs A 2014 High gain, low noise, fully complementary logic inverter based on bi-layer WSe_2 field effect transistors *Appl. Phys. Lett.* **105** 083511
[9] Castellanos-Gomez A, van Leeuwen R, Buscema M, van der Zant H S J, Steele G A and Venstra W J 2013 Single-layer MoS_2 mechanical resonators *Adv. Mater.* **25** 6719–23
[10] Butler S Z *et al* 2013 Progress, challenges, and opportunities in two-dimensional materials beyond graphene *ACS Nano.* **7** 2898–926
[11] Consadori F and Frindt R F 1970 Crystal size effects on exciton absorption spectrum of WSe_2 *Phys. Rev.* B **2** 4893–6
[12] Docherty C J *et al* 2014 Ultrafast transient terahertz conductivity of monolayer MoS_2 and WSe_2 grown by chemical vapor deposition *ACS Nano* **8** 11147–53
[13] Aivazian G, Gong Z, Jones A M, Chu R, Yan J and Mandrus D G 2015 Magnetic control of valley pseudospin in monolayer WSe_2 *Nat. Phys.* **11** 148–52
[14] Arora A, Koperski M, Nogajewski K, Marcus J, Faugeras C and Potemski M 2015 Excitonic resonances in thin films of WSe_2: from monolayer to bulk material *Nanoscale* **7** 10421
[15] Fang H *et al* 2014 Strong interlayer coupling in van der Waals heterostructures built from single-layer chalcogenides *Proc. Natl Acad. Sci. USA* **111** 6198–202
[16] Mak K F and Shan J 2016 Photonics and optoelectronics of 2D semiconductor transition metal dichalcogenides *Nat. Photon.* **10** 216–26
[17] Eda G, Yamaguchi H, Voiry D, Fujita T, Chen M and Chhowalla M 2011 Photoluminescence from chemically exfoliated MoS_2 *Nano Lett.* **11** 5111–6
[18] King L A, Zhao W, Chhowalla M, Riley D J and Eda G 2013 Photoelectrochemical properties of chemically exfoliated MoS_2 *J. Mater. Chem.* A **1** 8935
[19] Browning P 2015 Large-area synthesis of WSe_2 from WO_3 by selenium–oxygen ion exchange *2D Mater.* **2** 014003
[20] Chen L, Liu B, Abbas A N, Ma Y, Fang X, Liu Y and Zhou C 2014 Screw-dislocation-driven growth of two-dimensional few-layer and pyramid-like WSe_2 by sulfur-assisted chemical vapor deposition *ACS Nano* **8** 11543–51
[21] Yu J, Li J, Zhang W and Chang H 2015 Synthesis of high quality two-dimensional materials via chemical vapor deposition *Chem. Sci.* **6** 6705
[22] Huang J *et al* 2014 Large-area synthesis of highly crystalline WSe_2 monolayers and device applications *ACS Nano* **8** 923–30
[23] Su S *et al* 2014 Controllable synthesis of band-gap-tunable and monolayer transition-metal dichalcogenide alloys *Front. Energy Res.* **2** 27
[24] Li S *et al* 2015 Halide-assisted atmospheric pressure growth of large WSe_2 and WS_2 monolayer crystal *Appl. Mater. Today* **1** 60–6
[25] Eichfeld S M *et al* 2015 Highly scalable, atomically thin WSe_2 grown via metal organic chemical vapor deposition *ACS Nano* **9** 2080–7
[26] Thripuranthaka M, Kashid R V, Rout C S and Late D J 2014 Temperature dependent Raman spectroscopy of chemically derived few layer MoS_2 and WS_2 nanosheets *Appl. Phys. Lett.* **104** 081911
[27] Nicolosi V, Chhowalla M, Kanatzidis M G, Strano M S and Coleman J N 2013 Liquid exfoliation of layered materials *Science* **340** 1420
[28] Lee K, Kim H, Lotya M, Coleman J N, Kim G-T and Duesberg G S 2011 Electrical characteristics of molybdenum disulfide flakes produced by liquid exfoliation *Adv. Mater.* **23** 4178–82
[29] Coleman J N *et al* 2011 Two-dimensional nanosheets produced by liquid exfoliation of layered materials *Science* **331** 568–71
[30] Feng Q *et al* 2014 Growth of large-area 2D $MoS_{2(1-x)}Se_{2x}$ semiconductor alloys *Adv. Mater.* **26** 2648–53
[31] Cheng R *et al* 2014 Electroluminescence and photocurrent generation from atomically sharp WSe_2/MoS_2 heterojunction *p–n* diodes *Nano Lett.* **14** 5590–7
[32] van der Zande A M, Huang P Y, Chenet D A, Berkelbach T C, You Y, Lee G-H, Heinz T F, Reichman D R, Muller D A and Hone J C 2013 Grains and grain boundaries in highly crystalline monolayer molybdenum disulphide *Nat. Mater.* **12** 554–61
[33] Zhang Y *et al* 2013 Controlled growth of high-quality monolayer WS_2 layers on sapphire and imaging its grain boundary *ACS Nano* **7** 8963–71
[34] He K, Kumar N, Zhao L, Wang Z, Mak K F, Zhao H and Shan J 2014 Tightly bound excitons in monolayer WSe_2 *Phys. Rev. Lett.* **113** 026803
[35] Cui Q, Ceballos F, Kumar N and Zhao H 2014 Transient absorption microscopy of monolayer and bulk WSe_2 *ACS Nano* **8** 2970–6
[36] Li H *et al* 2013 Rapid and reliable thickness identification of two-dimensional nanosheets using optical microscopy *ACS Nano* **7** 10344–53
[37] Tonndorf P *et al* 2013 Photoluminescence emission and Raman response of monolayer MoS_2, $MoSe_2$, and WSe_2 *Opt. Express* **21** 4908–16
[38] Desai S B *et al* 2014 Strain-induced indirect to direct bandgap transition in multilayer WSe_2 *Nano Lett.* **14** 4592–7
[39] Yan T, Qiao X, Liu X, Tan P and Zhang X 2014 Photoluminescence properties and exciton dynamics in monolayer WSe_2 *Appl. Phys. Lett.* **105** 101901
[40] Wang G *et al* 2014 Valley dynamics probed through charged and neutral exciton emission in monolayer WSe_2 *Phys. Rev.* B **90** 075413
[41] Ghosh K and Singisetti U 2015 Thermoelectric transport coefficients in mono-layer MoS_2 and WSe_2: role of substrate, interface phonons, plasmon, and dynamic screening *J. Appl. Phys.* **118** 135711
[42] Zhang R, Koutsos V and Cheung R 2016 Elastic properties of suspended multilayer WSe_2 *Appl. Phys. Lett.* **108** 042104
[43] Chiu M *et al* 2014 Spectroscopic signatures for interlayer coupling in MoS_2–WSe_2 van der Waals stacking *ACS Nano* **8** 9649–56
[44] Hao K *et al* 2016 Direct measurement of exciton valley coherence in monolayer WSe_2 *Nat. Phys.* **12** 277–83
[45] Kim K *et al* 2015 Band alignment in WSe_2 graphene heterostructures *ACS Nano* **9** 4527–32
[46] Seyler K L *et al* 2015 Electrical control of second-harmonic generation in a WSe_2 monolayer transistor *Nat. Nanotechnol.* **10** 407–11
[47] Massicotte M, Schmidt P, Vialla F, Watanabe K, Taniguchi T, Tielrooij K J and Koppens F H L 2016 Photo-thermionic effect in vertical graphene heterostructures *Nat. Commun.* **7** 12174
[48] Jones A M *et al* 2013 Optical generation of excitonic valley coherence in monolayer WSe_2 *Nat. Nanotechnol.* **8** 634–8
[49] You Y, Zhang X, Berkelbach T C, Hybertsen M S, Reichman D R and Heinz T F 2015 Observation of biexcitons in monolayer WSe_2 *Nat. Phys.* **11** 477–82

[50] Zhang X, You Y, Zhao S Y F and Heinz T F 2015 Experimental evidence for dark excitons in monolayer WSe_2 *Phys. Rev. Lett.* **115** 257403
[51] Xu K, Wang Z, Du X, Safdar M, Jiang C and He J 2013 Atomic-layer triangular WSe_2 sheets: synthesis and layer-dependent photoluminescence property *Nanotechnology* **24** 465705
[52] He K, Poole C, Mak K F and Shan J 2013 Experimental demonstration of continuous electronic structure tuning via strain in atomically thin MoS_2 *Nano Lett.* **13** 2931–6
[53] Frindt R F 1963 The optical properties of single crystals of WSe_2 and $MoTe_2$ *J. Phys. Chem. Solids* **24** 1107–12
[54] Yu Y *et al* 2016 Engineering substrate interactions for high luminescence efficiency of transition-metal dichalcogenide monolayers *Adv. Funct. Mater.* **26** 4733–9
[55] Rigosi A F, Hill H M, Li Y, Chernikov A and Heinz T F 2015 Probing interlayer interactions in transition metal dichalcogenide heterostructures by optical spectroscopy: MoS_2/WS_2 and $MoSe_2/WSe_2$ *Nano Lett.* **15** 486–91
[56] Kleinman D A and Miller R C 1985 Band-gap renormalization in semiconductor quantum wells containing carriers *Phys. Rev.* B **32** 2266–72
[57] Chernikov A, Ruppert C, Hill H M, Rigosi A F and Heinz T F 2015 Population inversion and giant bandgap renormalization in atomically thin WS_2 layers *Nat. Photon.* **9** 466–71
[58] Amani M *et al* 2015 Near-unity photoluminescence quantum yield in MoS_2 *Science* **350** 1065–8
[59] Man M K L *et al* 2016 Protecting the properties of monolayer MoS2 on silicon based substrates with an atomically thin buffer *Sci. Rep.* **6** 20890
[60] Kang K N, Godin K and Yang E 2015 The growth scale and kinetics of WS_2 monolayers under varying H_2 concentration *Sci. Rep.* **5** 13205
[61] Godin K, Kang K N, Fu S and Yang E 2016 Increased monolayer domain size and patterned growth of WS_2 through controlling surface energy of substrates *J. Phys. D: Appl. Phys.* **49** 325304
[62] Gao L, Lemarchand F and Lequime M 2013 Refractive index determination of SiO_2 layer in the UV/Vis/NIR range: spectrophotometric reverse engineering on single and bi-layer designs *J. Eur. Opt. Soc.* **8** 13010
[63] Malitson I H and Dodge M J 1972 Refractive index and birefringence of synthetic sapphire *J. Opt. Soc. Am.* **62** 1405
[64] Dodge M J 1984 Refractive properties of magnesium fluoride *Appl. Opt.* **23** 1980–5
[65] Philipp H R 1973 Optical properties of silicon nitride *J. Electrochim. Soc.* **120** 295–300
[66] Gielisse P J, Mitra S S, Plendl J N, Griffis R D, Mansur L C, Marshall R and Pascoe E A 1967 Lattice infrared spectra of boron nitride and boron monophosphide *Phys. Rev.* **155** 1039
[67] Rubio-Bollinger G *et al* 2015 Enhanced visibility of MoS_2, $MoSe_2$, WSe_2 and black-phosphorus: making optical identification of 2D semiconductors easier *Electronics* **4** 847–56
[68] Godde T *et al* 2016 Exciton and trion dynamics in atomically thin $MoSe_2$ and WSe_2: effect of localization *Phys. Rev.* B **94** 165301
[69] Morell N, Reserbat-Plantey A, Tsioutsios I, Schädler K G, Dubin F, Koppens F H L and Bachtold A 2016 High quality factor mechanical resonators based on WSe_2 monolayers *Nano Lett.* **16** 5102–8
[70] El-Mahalawy S H and Evans B L 1976 The thermal expansion of 2H-MoS_2, 2H-$MoSe_2$ and 2H-WSe_2 between 20 and 800 °C *J. Appl. Crystallogr.* **9** 403–6
[71] Murray R and Evans B 1979 The thermal expansion of 2H-MoS_2 and 2H-WSe_2 between 10 and 320 K *J. Appl. Crystallogr.* **12** 312–5
[72] Su L, Yu Y, Cao L and Zhang Y 2015 Effects of substrate type and material-substrate bonding on high-temperature behavior of monolayer WS_2 *Nano Res.* **8** 2686–97
[73] Mitioglu A A, Galkowski K, Surrente A, Klopotowski L, Dumcenco D, Kis A, Maude D K and Plochocka P 2016 Magnetoexcitons in large area CVD-grown monolayer MoS_2 and $MoSe_2$ on sapphire *Phys. Rev.* B **93** 165412
[74] Huang J, Hoang T B and Mikkelsen M H 2016 Probing the origin of excitonic states in monolayer WSe_2 *Sci. Rep.* **6** 22414
[75] Lin Y, Ling X, Yu L, Huang S, Hsu A L, Lee Y-H, Kong J, Dresselhaus M S and Palacioś T 2014 Dielectric screening of excitons and trions in single-layer MoS_2 *Nano Lett.* **10** 5569
[76] Chernikov A, Berkelbach T C, Hill H M, Rigosi A, Li Y, Burak Aslan O, Reichman D R, Hybertsen M S and Heinz T F 2014 Exciton binding energy and nonhydrogenic Rydberg series in monolayer WS_2 *Phys. Rev. Lett.* **113** 076802
[77] Stier A V, Wilson N P, Clark G, Xu X and Crooker S A 2016 Probing the influence of dielectric environment on excitons in monolayer WSe_2: insight from high magnetic fields *Nano Lett.* **11** 7054
[78] Brener I, Olszakier M, Cohen E, Ehrenfreund E, Ron A and Pfeiffer L 1992 Particle localization and phonon sidebands in GaAs/Al_xGa_{1-x}As multiple quantum wells *Phys. Rev.* B **46** 7927
[79] Mouri S, Miyauchi Y, Toh M, Zhao W, Eda G and Matsuda K 2014 Nonlinear photoluminescence in atomically thin layered WSe_2 arising from diffusion-assisted exciton–exciton annihilation *Phys. Rev.* B **90** 155449
[80] Daniel C, Herz L M, Silva C, Hoeben F J M, Jonkheijm P, Schenning A P H J, and Meijer E W 2003 Exciton bimolecular annihilation dynamics in supramolecular nanostructures of conjugated oligomers *Phys. Rev.* B **68** 235212
[81] Castellanos-Gomez A, Buscema M, van der Zant H S J and Steele G A 2014 Deterministic transfer of two-dimensional materials by all-dry viscoelastic stamping *2D Mater.* **1** 011002
[82] Yu Y, Yu Y, Xu C, Barrette A, Gundogdu K and Cao L 2015 Fundamental limits of exciton-exciton annihilation for light emission in transition metal dichalcogenide monolayers *Phys. Rev.* B **93** 201111
[83] Huang Y *et al* 2015 Reliable exfoliation of large-area high-quality flakes of graphene and other two-dimensional materials *ACS Nano* **9** 10612–20